PHYSICAL REVIEW APPLIED **15,** 034031 (2021)

Quantum Sensing of Spin Fluctuations of Magnetic Insulator Films with Perpendicular Anisotropy

Eric Lee-Wong,[1,2] Jinjun Ding,[3] Xiaoche Wang,[1] Chuanpu Liu,[3] Nathan J. McLaughlin,[1]
Hailong Wang,[4] Mingzhong Wu,[3] and Chunhui Rita Du[1,4,*]

[1] *Department of Physics, University of California, San Diego, La Jolla, California 92093, USA*
[2] *Department of Nano Engineering, University of California, San Diego, La Jolla, California 92093, USA*
[3] *Department of Physics, Colorado State University, Fort Collins, Colorado 80523, USA*
[4] *Center for Memory and Recording Research, University of California, San Diego, La Jolla, California 92093, USA*

(Received 4 September 2020; revised 22 December 2020; accepted 12 February 2021; published 11 March 2021)

Nitrogen-vacancy (N-*V*) centers, optically active atomic defects in diamond, have been widely applied to emerging quantum sensing, imaging, and network efforts, showing unprecedented field sensitivity and nanoscale spatial resolution. Many of these advantages derive from their excellent quantum-coherence, single-spin addressability, and remarkable functionality over a broad temperature range, enabling opportunities to outperform their classical counterparts. To date, N-*V* measurements of spin fluctuations have mainly focused on systems with in-plane magnetization, but applications to material systems with a spontaneous out-of-plane magnetization remain largely unexplored despite their technological importance. Here, we report N-*V* sensing of intrinsic spin fluctuations of magnetic insulator $Y_3Fe_5O_{12}$ thin films with perpendicular magnetic anisotropy. The measured field dependence of N-*V* relaxation rates is well correlated to the variation of magnon density and band structure of the magnetic samples, which are challenging to access by the conventional magnetometry methods. Our results highlight the significant opportunities offered by N-*V* centers in diagnosing the noise environment of functional magnetic elements, providing valuable information to develop next-generation, high-density, and scalable spintronic devices.

DOI: 10.1103/PhysRevApplied.15.034031

I. INTRODUCTION

Magnetic thin films with perpendicular anisotropy are widely used for information processing and storage applications [1,2]. The spontaneous out-of-plane magnetization enables significant improvement of density, speed, and reliability in a variety of spin-based electronic devices, such as magnetic tunnel junctions [3], spin-torque nano-oscillators [4], and racetrack memory [5–7]. A range of material candidates including rare-earth and transition-metal alloys [8,9], $L1_0$-ordered (Co, Fe)–Pt alloys [10], and Co/(Pd, Pt) multilayers [11,12] have been extensively explored in this context. More recently, the material landscape has extended to insulators, e.g., $Y_3Fe_5O_{12}$ [13–15], $Tm_3Fe_5O_{12}$ [16–18], and $BaFe_{12}O_{19}$ thin films [19], whose perpendicular magnetic anisotropy (PMA) results from epitaxial strain or intrinsic magnetocrystalline anisotropy. In comparison with their metallic counterpart, spin information in magnetic insulators is carried by bosonic-type quasiparticles, namely magnons, enabling excellent spin-coherence length scale, extended spin lifetime, and reduced energy-dissipation channels. Taking advantage of these strengths, energy-efficient magnetic switching [16,17], fast domain-wall motions [6,7], large spin-pumping signals [20], and long-range spin-information transmission [21,22] have been demonstrated in a variety of insulating magnetic systems. In combination with desirable PMA and their highly tunable material properties, magnetic insulators promise to serve as a building block to revolutionize the current magnetic memory and storage technologies by enabling a significant improvement in energy consumption and functionality of present spintronic devices.

Despite these potential benefits, a direct measurement of the intrinsic spin fluctuations of insulating magnetic films with PMA is missing. In modern spintronic technologies, the magnitude and spatial profile of magnetic noise generated by a nanomagnet determine the density and scalability of miniaturized electronic devices [23,24]. On the other hand, the magnetic noise associated with the internal spin and magnon fluctuations is directly related to the underlying magnetic properties, such

---

[*] c1du@physics.ucsd.edu

as magnon-phonon interactions [25,26], magnon scattering [27–30], and magnon hydrodynamics [31]. Therefore, detailed information on the key material properties and device parameters can be extracted noninvasively by probing the intrinsic magnetic noise spectrum. Conventional magnetometry methods including vibrating sample magnetometer [32], superconducting quantum interference device (SQUID) [33], and ferromagnetic resonance (FMR) [34] are mainly designed to characterize the static and/or coherent dynamic magnetic properties, and are unable to access the noncoherent magnetic fluctuations. While some other methods such as magneto-optic-Kerr-effect microscopy [35–37] and Brillouin light-scattering spectroscopy [25–27,38] could detect the spontaneous magnetic fluctuations, their ultimate spatial resolution is limited by the optical diffraction limit. In addition, the field sensitivity of these conventional optical sensing tools is often compromised by interference effects [36], leading to an inability to reach the quantum limit to uncover low magnitude magnetic fields.

To address these challenges, we introduce nitrogen vacancy (N-V) centers [39], optically active atomic defects in diamond, to perform quantum sensing of perpendicularly magnetized $Y_3Fe_5O_{12}$ (YIG) thin films. A N-V center is formed by a nitrogen atom adjacent to a carbon-atom vacancy in one of the nearest-neighboring sites of a diamond crystal lattice [39]. The negatively charged N-V state has a $S = 1$ electron spin and serves as a three-level qubit system. Due to their excellent quantum coherence and single-spin sensitivity, N-V centers have been successfully applied to study the local temperature of a living cell [40], individual nuclear and electron-spin behaviors on the diamond surface [41,42], and correlated-electron systems [43], showing unprecedented field sensitivity and nanoscale spatial resolution [44,45]. In addition, a N-V center itself serves as a single-spin quantum bit with remarkable functionality over a broad temperature range. The dipolar coupling between N-Vs, magnons, and optical (microwave) photons offer an alternative way to develop hybrid quantum architectures for next-generation information technologies [46–50]. Exploiting this cutting-edge quantum metrology, we observe significantly enhanced N-V spin relaxation induced by the fluctuating dipolar stray fields generated by thermal magnons in PMA YIG thin films. The measured field-dependent N-V relaxation rates are well explained by the variation of the magnon density and band structure of the samples. The sensitivity length scale of the presented quantum-sensing platform is determined by the N-V-to-sample distance, which can ultimately approach the tens-of-nanometer regime by using scanning N-V microscopy [51,52]. Our results highlight the significant opportunities offered by N-V centers in diagnosing intrinsic spin fluctuations in a broad range of functional magnetic systems.

II. STRUCTURAL AND MAGNETIC CHARACTERIZATIONS OF PMA YIG FILMS

We start by discussing the structural and magnetic properties of the epitaxial YIG thin films with PMA. The YIG films are grown on single-crystal (111) $Gd_3(Sc_2Ga_3)O_{12}$ (GSGG) substrates by radio-frequency sputtering. Detailed information of the growth conditions has been reported in previous work [14]. Figure 1(a) shows the representative $\theta-2\theta$ x-ray diffraction scans of a series of YIG films with different thicknesses and a GSGG substrate. The two main peaks around 50.4° correspond to the (444) peaks of the GSGG substrate. The appearance of the two (444) peaks results from the coexistence of the $K_{\alpha 1}$ and $K_{\alpha 2}$ components of the x ray. The black arrows indicate the positions of the (444) peak of the YIG films, which clearly deviate from the bulk value as marked by the vertical dashed line. The lattice constant of GSGG is 12.554 Å, which is slightly larger than the bulk value of YIG of 12.376 Å. The tensile strain provided by the GSGG substrate induces a substantial out-of-plane magnetocrystalline anisotropy in the YIG thin film, which rotates the magnetic easy axis from in-plane (IP) to out-of-plane (OOP) direction. Figure 1(b) shows the field-dependent magnetization of 8-nm- and 12-nm-thick YIG thin films measured with an external magnetic field H applied in the OOP direction. The paramagnetic background of the GSGG substrate is subtracted. The nearly square hysteresis loop with a high remnant-to-saturation magnetization ratio demonstrates the PMA of the YIG thin films. An atomic force microscopy image in Fig. 1(c) shows a smooth surface of the YIG(8 nm)/GSGG sample with a roughness of 0.12 nm.

The strong PMA will change the effective magnetization $4\pi M_{\text{eff}}$ of the YIG thin films as follows: $4\pi M_{\text{eff}} = 4\pi M_s - H_\perp$ [13], where $4\pi M_s$ is the saturation magnetization and $H_\perp$ is the effective PMA field. To quantitatively characterize this effect, we perform angle- and frequency-dependent FMR measurements to extract $4\pi M_{\text{eff}}$ of the prepared YIG/GSGG samples. Figure 2(a) shows two representative FMR spectra of the 8-nm-thick PMA YIG film measured at a microwave frequency $f = 10$ GHz and a polar angle $\theta_H = 0$ and 90°. Here, θ_H is defined as the angle between the normal of the film plane and the external magnetic field. A significantly lower FMR resonant field H_{res} measured when $\theta_H = 0°$ confirms the OOP-oriented magnetic easy axis. Figure 2(b) shows the angular dependence of H_{res} for 8- and 12-nm PMA YIG thin films measured at $f = 10$ GHz. By fitting to Fig. 2(b), the effective magnetization $4\pi M_{\text{eff}}$ of YIG(8 nm)/GSGG and YIG(12 nm)/GSGG is extracted to be -456 ± 7 G and -1489 ± 10 G, respectively (see Appendix B for details). The negative sign results from the strong PMA, which overcomes the intrinsic YIG magnetization and dictates the magnetic easy axis. We also measure the frequency-dependent H_{res} of the PMA YIG films in both OOP and IP

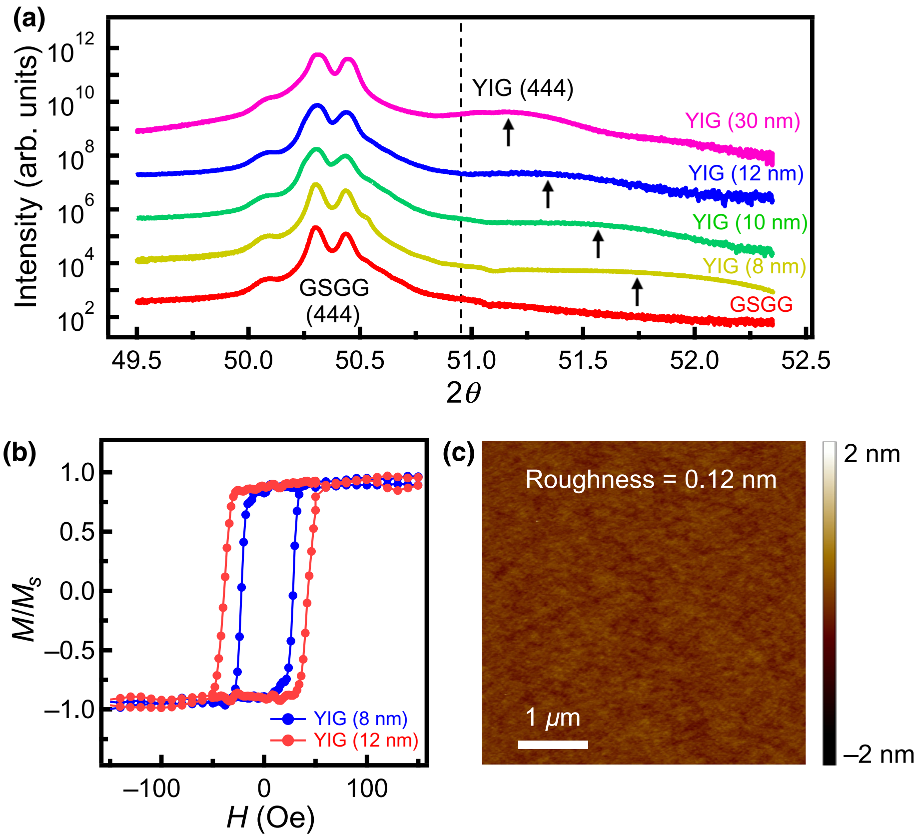

FIG. 1. (a) X-ray diffraction θ-2θ scan of 8-nm-, 10-nm-, 12-nm-, and 30-nm-thick YIG films grown on GSGG (111) substrates. The XRD data of a substrate is also shown for comparison. The curves are offset for clarity. (b) Out-of-plane magnetic hysteresis loops for YIG(8 nm)/GSGG and YIG(12 nm)/GSGG samples. (c) Atomic force microscopy image of an 8-nm-thick YIG film grown on GSGG (111) over an area of 5 μm × 5 μm, showing a surface roughness of 0.12 nm.

field geometries, as shown in Fig. 2(c). The measurement results can be well fitted to the Kittel equations: $f = \gamma/2\pi\,(H - 4\pi M_{\text{eff}})$ ($\theta_H = 0°$) and $f = (\gamma/2\pi)\sqrt{H(H + 4\pi M_{\text{eff}})}$ ($\theta_H = 90°$), where γ is the absolute gyromagnetic ratio of the magnetic sample. The obtained $4\pi M_{\text{eff}}$ is in agreement with the angle-dependent FMR measurement results. In order to determine the Gilbert damping of the YIG thin films, we measure the frequency dependence of the FMR linewidth ΔH_{FMR}, as shown in Fig. 2(d). In all cases, ΔH_{FMR} increases linearly with f. The Gilbert-damping constant α and the inhomogeneous linewidth broadening ΔH_{inh} can be obtained using equation [53,54]:

$$\Delta H_{\text{FMR}} = \Delta H_{\text{inh}} + \frac{4\pi\alpha f}{\sqrt{3}\gamma}. \tag{1}$$

Table I summarizes the obtained magnetic properties of the 8-nm- and 12-nm-thick YIG films grown on GSGG (111) substrates. Our N-V quantum-sensing measurements mainly focus on these two samples showing a large variation of the effective magnetization.

III. N-V-BASED QUANTUM-SENSING MEASUREMENTS OF PMA YIG FILMS

Next, we employ N-V centers to perform local sensing of the intrinsic spin fluctuations of the YIG(8 nm)/GSGG sample. Figure 3(a) illustrates the material and device structure for our N-V-based quantum-sensing measurements. A patterned diamond nanobeam [28,55,56] containing single N-V spins is mechanically transferred onto the surface of a YIG/GSGG sample. The diamond nanobeam has the shape of an equilateral triangular prism with dimensions of 500 nm × 500 nm × 10 μm. It is in van der Waals contact with the sample surface, ensuring nanoscale proximity between N-V centers and the YIG film. A PL image [Fig. 3(b)] shows individual N-V centers positioned on top of the sample surface, demonstrating single-spin addressability of our confocal measurement system. An external magnetic field is applied and aligned to the N-V axis with an angle $\theta_{\text{N}-V}$ relative to the surface normal.

At thermal equilibrium, transverse spin fluctuations of YIG magnons generate dipolar stray fields at the N-V site. When the frequency of YIG thermal magnons matches the N-V electron-spin-resonance (ESR) frequency, the magnetic noise will induce N-V spin transitions from the $m_s = 0$ to the $m_s = \pm 1$ states, leading to an enhanced N-V relaxation rate (see Appendix E for details) [28,57]:

$$\Gamma_\pm = \frac{k_B T}{f_\pm h} \int D(f_\pm, \mathbf{k}) f(\mathbf{k}, d)\, d\mathbf{k}, \tag{2}$$

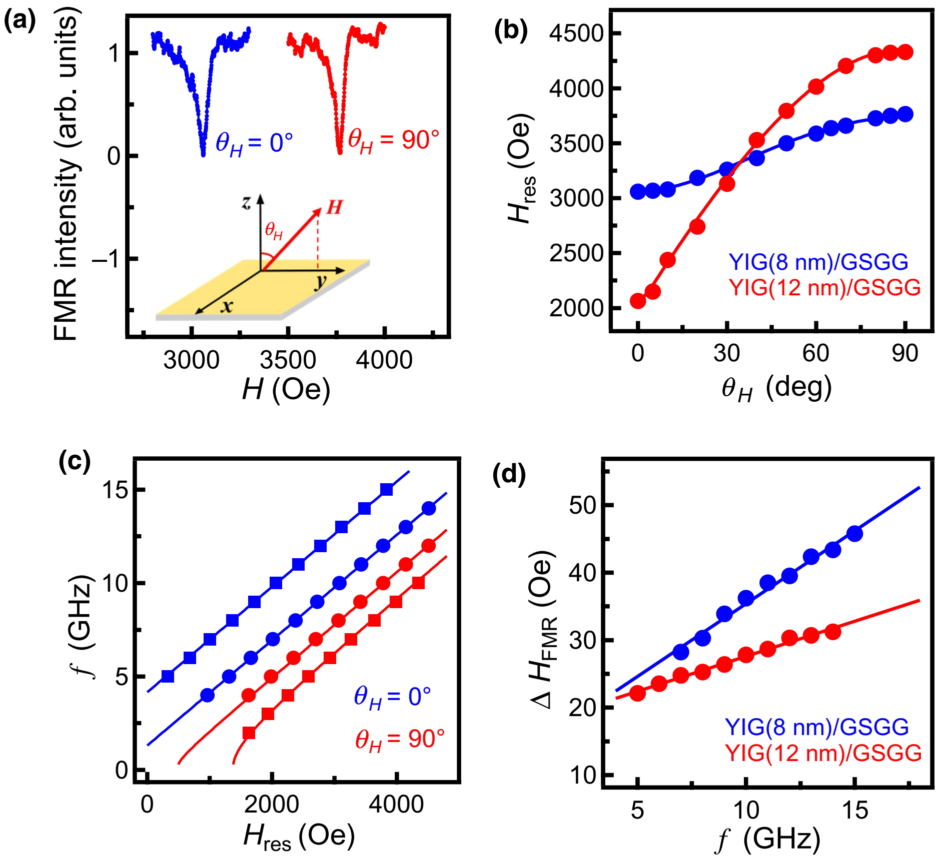

FIG. 2. (a) Two representative FMR spectra (in arbitrary unit) at a frequency $f = 10$ GHz for the 8-nm-thick YIG film grown GSGG (111). The red and blue curves correspond to in-plane and out-of-plane magnetic field geometries, respectively. (b) Angular dependence of the obtained FMR resonant field $H_{\rm res}$ for YIG(8 nm)/GSGG (blue points) and YIG(12 nm)/GSGG (red points). The curves are fittings to extract the effective magnetization. (c) Frequency dependence of $H_{\rm res}$ for YIG(8 nm)/GSGG (dots) and YIG(12 nm)/GSGG (squares) measured in both in-plane (red color) and out-of-plane (blue color) field geometries. The red and blue curves are fittings to Kittel equations. (d) Frequency dependence of FMR linewidth $\Delta H_{\rm FMR}$ for 8-nm (blue points) and 12-nm (red points) PMA YIG films. The red and blue curves are linear fittings to extract Gilbert damping and inhomogeneous contribution to $\Delta H_{\rm FMR}$.

where $f_\pm$ and $\Gamma_\pm$ are the N-V ESR frequencies and N-V relaxation rates of the $m_s = 0 \leftrightarrow \pm 1$ transitions, respectively, T is the temperature, k_B is the Boltzmann constant, h is the Planck constant, $D(f_\pm, \mathbf{k})$ is magnon spectral density, $\mathbf{k}$ is the magnon wave vector, and $f(\mathbf{k}, d)$ is the transfer function describing magnon-generated stray fields at the N-V site. Due to the "filtering" effect of $f(\mathbf{k}, d)$, a N-V center is mostly sensitive to magnetic noise with a wave vector $k \sim 1/d$, where d characterizes the distance between the surface of the magnetic sample and the N-V spin (see Appendix E for details). The magnetic fields with a smaller wave vector are algebraically suppressed and vanish at $k = 0$, which is expected because a uniform magnetization generates zero stray field. When k is larger than $1/d$, the dipolar fields are exponentially suppressed with an increasing k due to the self-averaging of short-wavelength fluctuations.

Experimentally, we employ N-V relaxometry measurements [28,29,58] to detect the spin fluctuations of the PMA YIG samples. The top panel of Fig. 3(c) shows the optical and microwave measurement sequence. A green laser pulse is first applied to initialize the N-V spin to the $m_s = 0$ state. The spin noise generated by YIG magnons at frequencies $f_\pm$ induces N-V spin transitions from the $m_s = 0$ to the $m_s = \pm 1$ states. After a delay time t, we measure the occupation probabilities of the N-V spin at the $m_s = 0$ and the $m_s = \pm 1$ states by applying a microwave π pulse on the corresponding ESR frequencies and measuring the spin-dependent PL during the green-laser read-out pulse. By measuring the integrated PL intensity as a function of the delay time t, N-V relaxation rates can be quantitatively obtained by fitting to a three-level model (see Appendix D for details) [28,57]. The bottom panel of Fig. 3(c) shows two sets of N-V spin-relaxation data measured with $H = 345$ Oe and 459 Oe. The measured PL intensity corresponding to the $m_s = 0$ (± 1) state decreases (increases) as a function of t, demonstrating the magnetic-noise-induced relaxation of the N-V spin to a mixture of the $m_s = 0$ and the $m_s = \pm 1$ states.

Figure 3(d) shows the obtained N-V spin-relaxation rates $\Gamma_\pm$ as a function of H. The results can be well fitted by Eq. (2), by which the N-V-to-sample distance d is obtained to be 239 ± 11 nm. Notably, Γ_- corresponding to the

TABLE I. Magnetic properties of YIG thin films grown on GSGG substrates.

Thickness (nm)	$4\pi M_{\rm eff}$ (*G*)	Gilbert damping α ($\times 10^{-3}$)	Inhomogeneous linewidth broadening $\Delta H_{\rm inh}$ (Oe)
8	-456 ± 7	5.2 ± 0.2	13.8 ± 1.1
12	-1489 ± 10	2.5 ± 0.1	17.2 ± 0.4

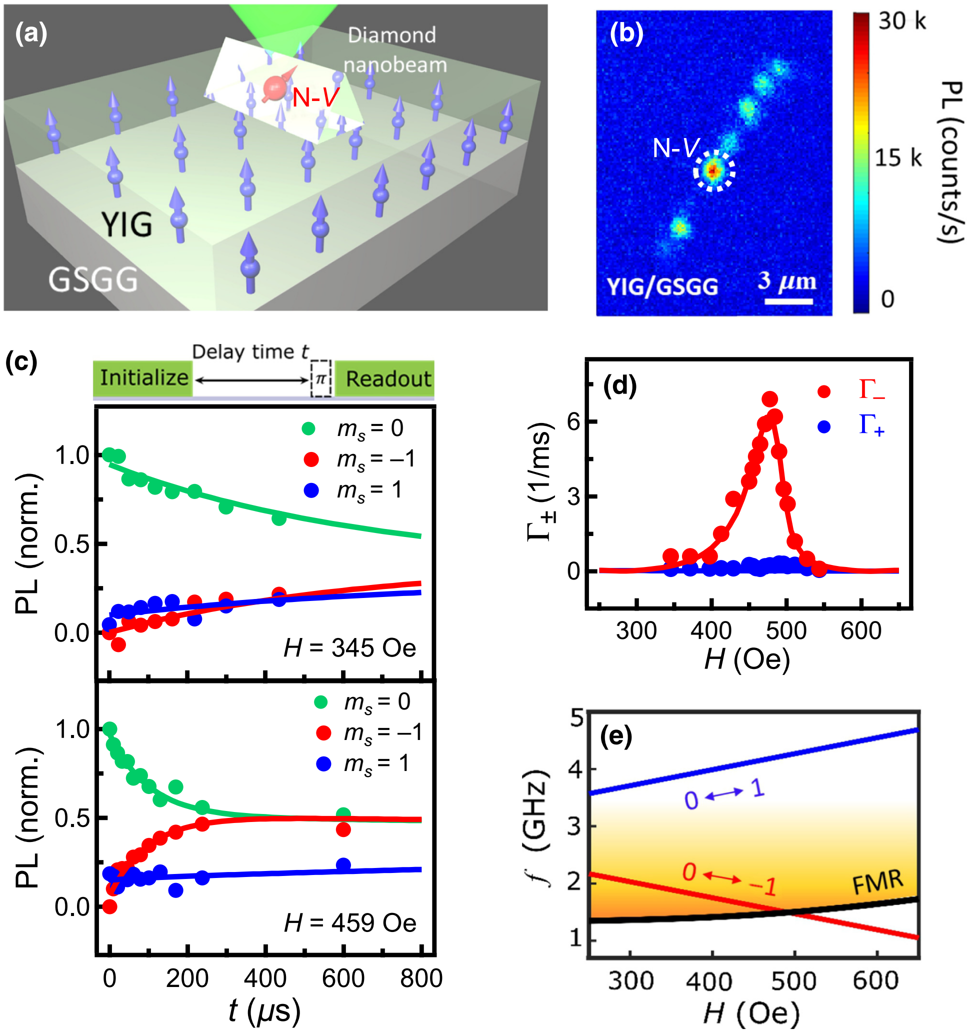

FIG. 3. (a) Schematic of a single N-V spin contained in a patterned diamond nanobeam locally probing the spin fluctuations of a PMA YIG thin-film grown on a GSGG substrate. (b) PL image showing individually addressable N-V spins positioned on top of the sample surface. (c) Top panel: optical and microwave sequence for N-V relaxometry measurements. Bottom panel: two sets of N-V relaxation data measured with $H = 345$ and 459 Oe for an 8-nm-thick YIG film grown GSGG. (d) N-V spin-relaxation rate Γ_+ (blue points) and Γ_- (red points) measured as a function of H. The solid lines are fitting to Eq. (2), which gives the N-V-to-sample distance of 239 ± 11 nm. (e) Sketch of the magnon density of the YIG (8 nm)/GSGG sample and the N-V ESR frequencies $f_{\pm}$ as a function of H.

$m_s = 0 \leftrightarrow -1$ transition exhibits a significant variation with H and shows a maximum around $H = 477$ Oe. In contrast, the magnitude of Γ_+ corresponding to the $m_s = 0 \leftrightarrow +1$ transition is orders of magnitude smaller in comparison with Γ_-. The variation of the measured N-V relaxation rates is correlated to the field-dependent magnon density of the sample and the N-V ESR frequencies $f_{\pm}$. Figure 3(e) plots the magnon density of the 8-nm-thick YIG thin film and $f_{\pm}$ as a function of H. The magnon density at a given frequency f can be calculated by multiplying the Bose-Einstein distribution function $1/[exp(fh/k_BT) - 1]$ by the magnon density of state. The magnon density of state is a constant in the two-dimensional limit, which is appropriate for the ultrathin films studied in our experiments. At room temperature where $k_BT \gg fh$, the Bose-Einstein distribution function $1/[exp(fh/k_BT) - 1]$ evolves to the Rayleigh-Jeans distribution function k_BT/fh. Therefore, the magnon density falls off as $1/f$ as indicated by the fading color. The minimal magnon band is determined by the FMR frequency f_{FMR}, which is calculated by the magnon dispersion relationship with $\theta_{\mathrm{N}-V} = 72°$ (see Appendix C for details). Due to the Zeeman splitting, the N-V ESR frequencies $f_{\pm}$ vary with the external magnetic field as follows: $f_{\pm} = 2.87 \pm \tilde{\gamma} H/2\pi$, where $\tilde{\gamma}$ is the gyromagnetic ratio of the N-V spin. As H increases, the lower branch of the N-V ESR frequency f_- decreases and probes the YIG thermal magnons with a higher density, leading to a significant enhancement of Γ_-, as shown in Fig. 3(d). The maximal Γ_- emerges at $H \sim 477$ Oe, where f_- corresponds to the peak regime of the "filter function" (see Appendix D for details). When $H > 492$ Oe, f_- lies below the minimum of YIG magnon band. The measured Γ_- rapidly decays, indicating effective suppression of spin noise generated at frequency f_-. For the upper branch of the N-V ESR frequency f_+, it probes YIG thermal magnons with higher frequencies, lower magnon densities, and wave vectors falling outside the N-V sensitivity regime. Therefore, Γ_+ is orders of magnitude smaller than Γ_- and does not exhibit a significant variation with H.

The magnetic properties of perpendicularly magnetized YIG thin films are usually sensitive to epitaxial strain, thickness, and detailed growth parameters, as shown in

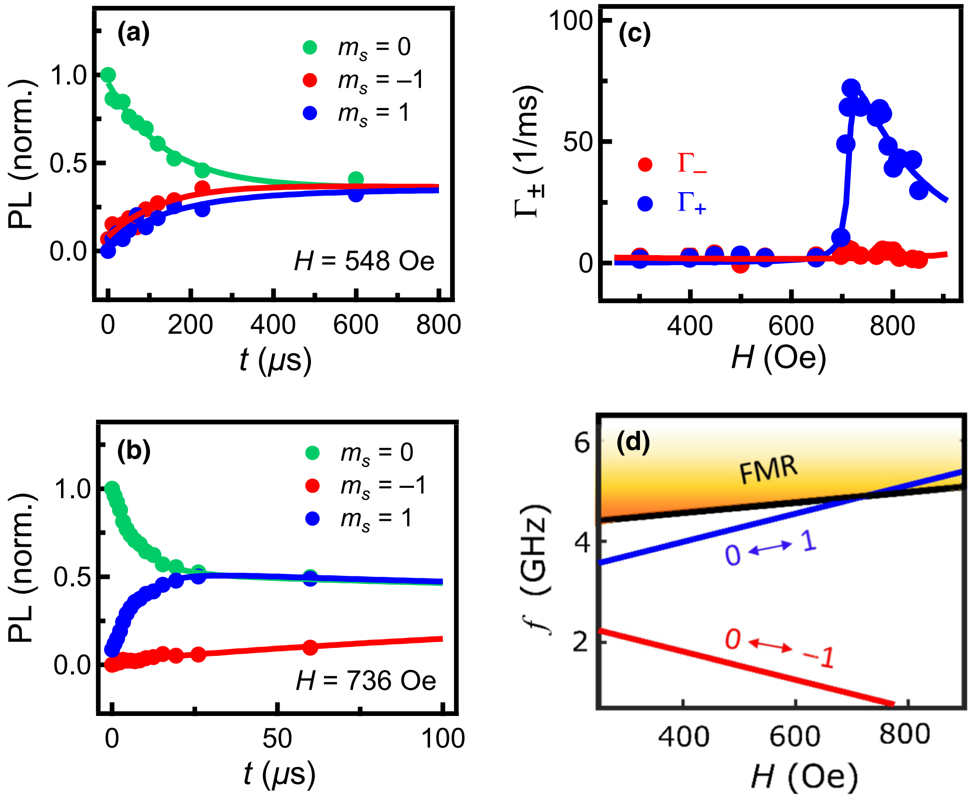

FIG. 4. (a), (b) Two sets of N-*V* relaxation data measured with $H = 548$ and 736 Oe for a 12-nm-thick YIG film grown a GSGG substrate. (c) N-*V* spin-relaxation rate Γ_+ (blue points) and Γ_- (red points) measured as a function of *H*. The solid lines are fitting to Eq. (2), which gives the N-*V*-to-sample distance of 114 ± 10 nm. (d) Sketch of the magnon density of the YIG(12 nm)/GSGG sample and the N-*V* ESR frequencies $f_\pm$ as a function of *H*.

Table I. To illustrate the versatility of the N-*V* quantum-sensing platform, we also apply N-*V* relaxometry measurements to the YIG(12 nm)/GSGG sample, whose zero-field magnon band gap is larger than the corresponding N-*V* ESR frequency. Figures 4(a) and 4(b) show two sets of N-*V* spin-relaxation data measured with $H = 548$ and 736 Oe, respectively. The extracted field-dependent N-*V* relaxation rates $\Gamma_\pm$ are plotted in Fig. 4(c). Due to the significantly enhanced PMA ($4\pi M_{\text{eff}} = -1489 \pm 10$ *G*), the minimal magnon energy f_{FMR} of the 12-nm-thick PMA YIG film is 3.9 GHz, which is above $f_\pm = 2.87$ GHz when $H = 0$. As *H* increases, f_- always lies below the magnon band minimum, thus, giving rise to a negligible N-*V* relaxation rate Γ_-, as shown in Fig. 4(c). In contrast, the upper branch of the N-*V* ESR frequency f_+ increases faster than f_{FMR} and crosses with the magnon band minimum at $H = 727$ Oe [Fig. 4(d)], accompanied with a dramatic enhancement of Γ_+. Note that the measured maximal N-*V* relaxation rate is about one order of magnitude larger than the value observed in the case of the 8-nm-thick YIG sample, which mainly results from a closer N-*V*-to-sample distance ($d = 114 \pm 10$ nm). As f_+ further increases, the N-*V* relaxation rate Γ_+ starts to decay due to a reduced magnon density and the "filtering" effect of the wave vector [28,57]. We highlight that the magnetic anisotropy of the PMA YIG thin films can be systematically controlled by thickness, strain, and chemical doping [13–15], leading to an effective tuning of the magnon band gap across the N-*V* ESR frequency. For certain PMA magnets, their magnetic anisotropy could be further manipulated electrically [59], which provides a tuning knob to switch "on" and "off" the coupling between an N-*V* center and thermal magnons [60,61]. These potential benefits underline the opportunity offered by PMA magnetic films for developing N-*V*-based hybrid quantum electronic devices.

Finally, we note that the presented N-*V* relaxometry measurements can also be employed to diagnose intrinsic material properties such as the effective magnetization $4\pi M_{\text{eff}}$ and spin-wave exchange constant D_s. The $4\pi M_{\text{eff}}$ for the 8-nm and 12-nm PMA YIG thin films obtained by fitting the field dependence of $\Gamma_\pm$ [Figs. 3(d) and 4(c)] are -442 ± 7 *G* and -1470 ± 12 *G*, respectively, in excellent agreement with the conventional FMR measurement results as shown in Table II. The fitted spin-wave stiffness exchange constant D_s is 8.458×10^{-40} J m^2, and is in agreement with values reported in previous studies [62]. Our work confirms that the presented N-*V* quantum-sensing

TABLE II. Comparison of $4\pi M_{\text{eff}}$ of PMA YIG films obtained by FMR and N-*V* relaxometry measurements.

Thickness (nm) of PMA YIG films	$4\pi M_{\text{eff}}$ (*G*) obtained by FMR measurements	$4\pi M_{\text{eff}}$ (*G*) obtained by N-*V* measurements
8	-456 ± 7	-442 ± 7
12	-1489 ± 10	-1470 ± 12

platform could provide an alternative way to characterize the relevant material and device properties for practical applications.

IV. CONCLUSION

In summary, we demonstrate N-V centers as a local probe of the intrinsic spin fluctuations and relevant material properties of nanometer-thick PMA YIG thin films. The observed field-dependent N-V relaxation rates are well explained by the variation of the magnon density, magnon band gaps of the magnetic samples, and the N-V transfer function. In contrast to the conventional magnetic resonance techniques that mainly probe coherent spin-wave modes, we highlight that N-V relaxometry provides a unique way to access noncoherent magnon thermal fluctuations by which relevant material parameters such as magnon band minimum, intrinsic magnetic anisotropy, and spin-wave exchange constant can be quantitatively extracted. We expect that three-dimensional mapping of magnetic noise of functional spintronic devices can be ultimately achieved by employing scanning N-V microscopy [51,52]. The demonstrated coupling between perpendicularly magnetized ferromagnets and N-V centers may also find applications in developing solid-state-based hybrid quantum architectures for next-generation spintronic technologies [46–50].

ACKNOWLEDGMENTS

The work at UCSD is supported by the U.S. National Science Foundation under Award No. ECCS-2029558 and the Air Force Office of Scientific Research under Award No. FA9550-20-1-0319. The work at CSU is supported by the U.S. National Science Foundation under Grants No. EFMA-1641989, No. ECCS-1915849 and No. DMR-2002980.

APPENDIX A: SAMPLE INFORMATION

Epitaxial $Y_3Fe_5O_{12}$(YIG) thin films are grown by magnetron sputtering on $Gd_3(Sc_2Ga_3)O_{12}$ (GSGG) substrates at a base chamber pressure of approximately 2.0×10^{-8} Torr. Amorphous YIG films are first grown at room temperature at a rate of approximately 0.9 nm/min. The as-deposited YIG films are subsequently annealed at 900 °C in an oxygen environment for 3 h to crystallize. The growth details are reported in Ref. S1 [14]. The YIG films show a smooth surface condition as demonstrated by atomic force microscopy characterizations [Fig. 1(c)]. The perpendicular magnetic anisotropy is confirmed by vibrating sample magnetometry (VSM), angle- and frequency-dependent ferromagnetic resonance measurements.

Patterned diamond nanobeams [28,55] containing individually addressable N-V centers are transferred onto the surface of YIG thin films using a tungsten tip performed under a micromechanical transfer stage. The N-V spin state is controlled by microwave currents flowing a 10-μm-wide and 200-nm-thick on-chip Au stripline patterned on YIG films.

APPENDIX B: ANALYSIS OF ANGLE-DEPENDENT FERROMAGNETIC RESONANCE RESULTS

We perform angle-dependent FMR measurements to extract the effective magnetization $4\pi M_{\mathrm{eff}}$ and PMA $H_\perp$ of the PMA YIG films. When an external magnetic field **H** is applied at an angle θ_H relative to the surface normal, the equilibrium position of the YIG magnetization **M** can be obtained by minimizing the free energy F of the YIG film [63]:

$$F = -\mathrm{H}\cdot\mathbf{M} + \frac{1}{2}M(4\pi M_{\mathrm{eff}})\cos^2\theta_H, \tag{B1}$$

where $4\pi M_{\mathrm{eff}}{=}4\pi M_{\mathrm{s}}{-}H_\perp$ is the effective saturation magnetization including the shape anisotropy $4\pi M_s$ and $H_\perp$. Contributions from the higher-order magnetocrystalline antitropy are found to be negligible and are not being included in the above equation. The equilibrium orientation θ_H can be obtained by minimizing the free energy F and the FMR frequency is given by [64]

$$\left(\frac{\omega}{\gamma}\right)^2 = \frac{1}{M^2\sin^2\theta_H}\left[\frac{\partial^2 F}{\partial\theta_H{}^2}\frac{\partial^2 F}{\partial\phi^2} - \left(\frac{\partial^2 F}{\partial\theta_H\partial\phi}\right)^2\right], \tag{B2}$$

where $\omega = 2\pi f$ is the resonant frequency, γ is the absolute gyromagnetic ratio of the magnetic sample, and ϕ is the polar coordinate describing the orientation of the in-plane projection of $\boldsymbol{M}$. We use a numerical procedure to obtain the equilibrium angles at FMR resonance conditions. Fitting the angle-dependent magnetic resonance field H_{res}, $4\pi M_{\mathrm{eff}}$ is obtained to be -456 ± 7 G and -1489 ± 10 G for the 8-nm-thick and 12-nm-thick PMA YIG films, respectively.

APPENDIX C: CALCULATION OF MAGNON BAND MINIMUM OF PMA YIG THIN FILMS

In this section, we describe the method to calculate the magnon band minimum of YIG thin films for N-V measurements. Figure 5 shows a coordinate system used for analysis, where an external magnetic field H lies in the y-z plane. θ_H and θ_M characterize the angle of H and the YIG magnetization **M** relative to the z axis, respectively. In our N-V relaxometry measurements, H is applied along the N-V axis with $\theta_H = 72°$ and 61° for 8-nm- and 12-nm-thick YIG films, respectively. k and ϕ_k are polar coordinates describing the magnon wave vector **k**. We start from a general expression of the dispersion relationship of YIG spin wave modes as follows [65]:

$$\omega(k,\phi_k) = \sqrt{\left(\gamma B_M + \frac{D_s}{\hbar}k^2\right)\left(\gamma B_M + \frac{D_s}{\hbar}k^2 + \gamma\mu_0 M_{\mathrm{eff}} F(k,\phi_k)\right)}, \tag{C1}$$

where $\hbar$ is the reduced Planck constant, B_M is the internal field including contributions from H and the effective demagnetizing field $\mu_0 M_{\mathrm{eff}}\cos(\theta_M)$ generated by the out-of-plane component of the effective YIG magnetization, D_s is the spin-wave stiffness constant of YIG, μ_0 is the permeability in free space and

$$F(k,\phi_k) = P(k) + \sin^2(\theta_M)\Bigg(1 - P(k)(1+\cos^2\phi_k) + \gamma\mu_0 M_{\mathrm{eff}}\frac{P(k)[1-P(k)]\sin^2\phi_k}{\gamma B_M + \frac{D_s}{\hbar}k^2}\Bigg), \tag{C2}$$

where $P(k) = 1 - [(1-e^{-kt_{\mathrm{YIG}}})/kt_{\mathrm{YIG}}]$, t_{YIG} is the thickness of the YIG film. θ_M and B_M can be quantitatively obtained by solving the following equations:

$$B_M\cos(\theta_M) = H\cos(\theta_H) - \mu_0 M_{\mathrm{eff}}\cos(\theta_M), \tag{C3}$$

$$B_M\sin(\theta_M) = H\sin(\theta_H). \tag{C4}$$

For FMR with a wave vector $k = 0$, magnon dispersion is reduced to a simple formula:

$$\omega_{\mathrm{FMR}} = \gamma\sqrt{B_M[B_M + \mu_0 M_{\mathrm{eff}}\sin^2(\theta_M)]}. \tag{C5}$$

The field-dependent ω_{FMR} shown in Figs. 3(e) and 4(d) is obtained by solving Eqs. (C3)–(C5). Note that the magnon band minimum of nanometer-thick YIG thin films equals the FMR frequency ω_{FMR} over the field range studied in our experiments.

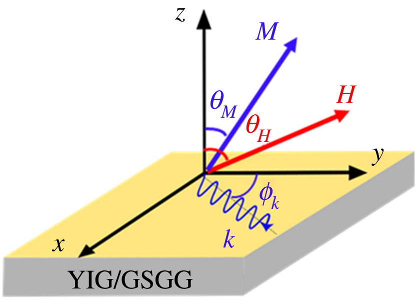

FIG. 5. The coordinate system used for the analysis of the magnon dispersion relationship of a YIG thin-film grown on a GSGG substrate.

APPENDIX D: MEASUREMENTS OF N-*V* RELAXATION RATES

A N-*V* center has a $S = 1$ electron spin and serves as a three-level quantum impurity. Figure 6(a) shows the energy levels of an N-*V* spin as a function of an external magnetic field H applied along the N-*V* axis. For $H = 0$, the $m_s = \pm 1$ states are degenerate and the corresponding electron-spin-resonance frequency equals 2.87 GHz. For $H > 0$, the Zeeman coupling separates the $m_s = -1$ and the $m_s = +1$ spin states by an energy gap equaling $2\gamma H$, where γ denotes the gyromagnetic ratio. This three-level spin system can be optically accessed by spin-dependent PL, where the $m_s = \pm 1$ spin states are more likely to be trapped by a nonradiative pathway (in the red wavelength range) through an intersystem crossing and back to the $m_s = 0$ ground state, yielding a significantly reduced PL intensity.

Fluctuating magnetic fields at the N-*V* ESR frequencies can induce $m_s = 0 \leftrightarrow \pm 1$ transitions as illustrated in Fig. 6(b), which can be optically accessed by N-*V* relaxometry measurements via spin-dependent PL. Our N-*V* measurements are performed in a home-built scanning confocal microscope. Laser pulses for optical initialization and read-out of the N-*V* spins are generated by an acoustic optical modulator in a double-pass configuration. The external magnetic field is generated by a cylindrical (Nd, Fe)B permanent magnet. The magnitude and the orientation of the magnetic fields at individual N-*V* sites can be systemically controlled by moving the position of the permanent magnet. Figure 3(c) in the main text shows two sets of N-*V* relaxation data measured with $H = 345$ and 459 Oe for an 8-nm-thick YIG film grown GSGG. To extract the N-*V* relaxation rates $\Gamma_\pm$, we fit the time-dependent PL data into the following equation, which is based on a three-level model [28,57]:

$$\frac{d}{dt}\begin{bmatrix} P_0(t) \\ P_+(t) \\ P_-(t) \end{bmatrix} = \begin{bmatrix} -(\Gamma_+ + \Gamma_-) & \Gamma_+ & \Gamma_- \\ \Gamma_+ & -\Gamma_+ & 0 \\ \Gamma_- & 0 & -\Gamma_- \end{bmatrix}\begin{bmatrix} P_0(t) \\ P_+(t) \\ P_-(t) \end{bmatrix}. \tag{D1}$$

Here, P_0, P_+, and P_- are the probabilities of an N-*V* spin at the $m_s = 0$, $m_s = +1$, and $m_s = -1$ states, respectively, Γ_+ and Γ_- characterize the spin-relaxation rates of the $m_s = 0 \leftrightarrow +1$ and $m_s = 0 \leftrightarrow -1$ transitions. Note that the magnetic noise generated by the YIG films will not affect the $m_s = +1 \leftrightarrow -1$ transition, therefore, the corresponding relaxation rate is zero. By fitting the results shown in Fig. 3(c) in the paper, we are able to extract the N-*V* relaxation rate $\Gamma_\pm$.

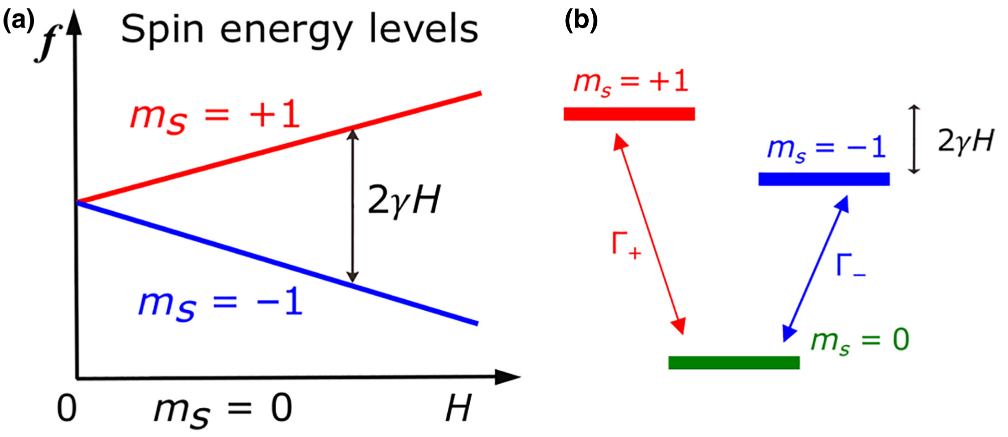

FIG. 6. (a) Energy diagram of a N-V spin as a function of an external field H applied along the N-V axis. (b) Schematic to illustrate the spin relaxation in a three-level quantum system.

APPENDIX E: NITROGEN-VACANCY RELAXATION RATES INDUCED BY TRANSVERSE SPIN FLUCTUATIONS

In this section, we provide detailed calculations of N-V relaxation rate induced by transverse spin fluctuations. We start from Eq. (2) in the main text [28]:

$$\Gamma_{\pm} = \frac{k_B T}{h f_{\pm}} \int D(f_{\pm},\ \mathbf{k}) f(\mathbf{k}, d) d\mathbf{k}, \tag{E1}$$

where $\Gamma_{\pm}$ characterize the N-V relaxation rates corresponding to the $m_s = 0$ to the $m_s = \pm 1$ states, the magnon spectral density

$$D(f_{\pm},\ \mathbf{k}) = \frac{1}{\pi} \frac{W}{W^2 + [\omega(k, \phi_k) - 2\pi f_{\pm}]^2}$$

is modeled as a Lorentzian function centered at the magnon dispersion $\omega(k, \phi_k)$, W characterizes the width of the FMR, and d is the N-V-to-sample distance. $f(\mathbf{k}, d)$ is the transfer function describing the magnon-generated noncoherent magnetic fields at the N-V site [28]:

$$f(\mathbf{k}, d) = C\, k e^{-2dk}(1 - e^{-2t_{\mathrm{YIG}}k}) \left[\sin^4(\phi_k) + \cos^2(\theta_H) \frac{\sin^2(2\phi_k)}{4} + \sin^2(\theta_H) \sin^2(\phi_k) \right], \tag{E2}$$

where C is a constant, θ_H is the angle of the N-V axis with respect to the surface normal. Note that the external magnetic field H is aligned with the N-V axis during N-V measurements. The term $ke^{-2dk}(1 - e^{-2t_{\mathrm{YIG}}k})$ is a "filter function" describing the selective sensitivity of the N-V spin to magnons within a certain range of wave vectors. The term between square brackets in Eq. (E2) calculates the component of the magnetic field that is perpendicular to the N-V axis. Substituting the full expression of $f(\mathbf{k}, d)$ and $D(f_{\pm},\ \mathbf{k})$ into Eq. (E1), we have [28]

$$\Gamma_{\pm} = C \frac{k_B T}{h f_{\pm}} \int \left[\sin^4(\phi_k) + \cos^2(\theta_H) \frac{\sin^2(2\phi_k)}{4} + \sin^2(\theta_{\mathrm{H}}) \sin^2(\phi_k) \right] \frac{W k e^{-2dk}(1 - e^{-2t_{\mathrm{YIG}}k})}{\pi \{ W^2 + [\omega(k, \phi_k) - 2\pi f_{\pm}]^2 \}} k dk d\phi_k. \tag{E3}$$

We use Eq. (E3) to fit the field-dependent N-V relaxation rate $\Gamma_{\pm}$, as shown in Figs. 3(d) and 4(c). The dependence on the external magnetic field H enters through the N-V ESR frequencies $f_{\pm} = 2.87 \pm \gamma H / 2\pi$ and the field-dependent magnon dispersion $\omega(k,\ \phi_k)$. The theoretical model agrees well with the measured N-V relaxation rates $\Gamma_{\pm}$, from which the N-V-to-sample distance d is determined to be 239 ± 11 nm and 114 ± 10 nm for 8-nm- and 12-nm-thick YIG films, respectively. Effective magnetization $4\pi M_{\mathrm{eff}}$ for the 8-nm and 12-nm PMA YIG films

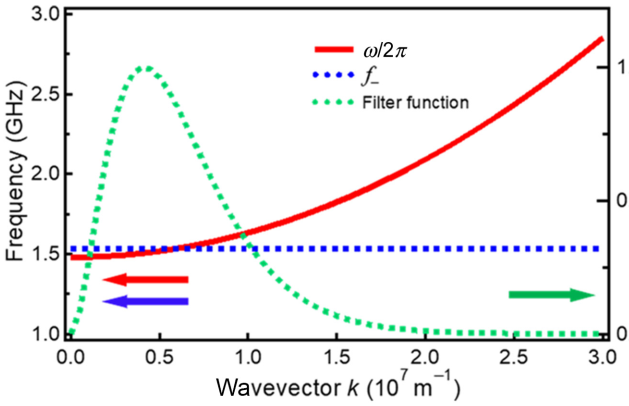

FIG. 7. Calculated magnon dispersion $\omega/2\pi$ (red curve) for the 8-nm-thick PMA YIG thin film at $H = 477$ Oe and $\theta_H = 72°$. The green dashed line plots the “filter function” as a function of wave vector k and the blue dashed line marks the lower branch of the N-V ESR frequency $f_- = 1.53$ GHz.

are obtained to be -442 ± 7 G and -1470 ± 12 G, respectively, in excellent agreement with the conventional FMR measurements as shown in Table II in the manuscript. The spin-wave stiffness constant D_s is fitted to be 8.458 $\times$ 10^{-40} J m^2, in agreement with the values reported in previous work [62].

Next, we use the data measured on the YIG(8 nm)/GSGG sample to illustrate the selective sensitivity of N-V centers to thermal magnons with a certain wave vector k. The green dashed line in Fig. 7 plots the “filter function” $k^2 e^{-2dk}(1 - e^{-2t_{\mathrm{YIG}}k})$ as a function of wave vector k (d is set to be 239 nm in the calculation), where the peak value emerges at $k = 1/d = 4.2 \times 10^{-6}$ m^{-1}. As shown in Fig. 3(d), the measured N-V relaxation rate Γ_- corresponding to the $m_s = 0 \leftrightarrow -1$ transition exhibits a maximal value around $H = 477$ Oe. The red curve in Fig. 7 plots the magnon dispersion $\omega/2\pi$ of the 8-nm-thick PMA YIG film at $H = 477$ Oe and $\theta_{\mathrm{H}} = 72°$. At this condition, the lower branch of the N-V ESR frequency f_- equals 1.53 GHz (blue dashed line shown in Fig. 7) and crosses with the dispersion curve at a wave vector $k \sim 5.5 \times 10^{-6}$ m^{-1}, which corresponds to the peak region of the “filter function.”

APPENDIX F: LOCAL MEASUREMENTS OF FERROMAGNETIC RESONANCE BY N-V RELAXOMETRY

Lastly, we show that the N-V relaxometry method can also be used to probe the local FMR of the PMA YIG thin films. The oscillating magnetic field used to excite FMR of the PMA YIG films is generated by microwave current flowing through the on-chip Au stripline. The top panel of Fig. 8 shows the optical and microwave measurement sequence. A green laser pulse is first applied to initialize the N-V spin to the $m_s = 0$ state. Next, a microwave pulse at a frequency f is applied, followed by a microwave π pulse and a green-laser read-out pulse to detect the occupation probabilities of the N-V spin [28,57]. Note that when f matches the FMR frequency f_{FMR} of the YIG thin film, a substantial amount of coherent magnons with a wave vector $k = 0$ can be generated, leading to enhanced magnon densities at the N-V ESR frequencies via multimagnon scattering processes [56]. The bottom panel of Fig. 8 plots the normalized N-V relaxation rate Γ_-/Γ_- ($f = 1.46$ GHz) measured on the YIG(8 nm)/GSGG sample as a function of f. The external magnetic field H is fixed at 455 Oe. Notably, the measured N-V relaxation rate increases by a factor of 4 at $f_{\mathrm{FMR}} = 1.49$ GHz, demonstrating the sensitivity of N-V centers to local coherent spin dynamics in a PMA YIG thin film.

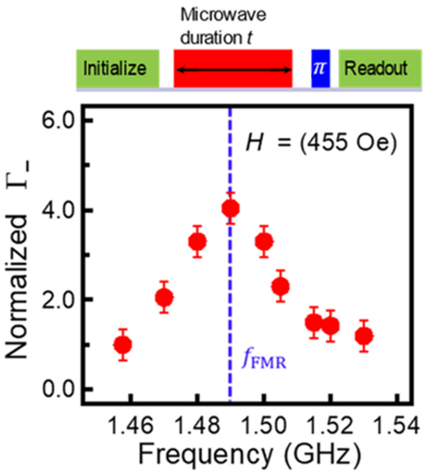

FIG. 8. Normalized N-V relaxation rate [Γ_-/Γ_- ($f = 1.46$ GHz)] measured as a function of the microwave frequency. The external magnetic field H is fixed at 455 Oe. The blue dashed line indicates the FMR frequency f_{FMR} of the 8-nm-thick PMA YIG thin film grown on the GSGG substrate.

[1] S. Ikeda, K. Miura, H. Yamamoto, K. Mizunuma, H. D. Gan, M. Endo, S. Kanai, J. Hayakawa, F. Matsukura, and H. Ohno, A perpendicular-anisotropy CoFeB-MgO magnetic tunnel junction, Nat. Mater. **9**, 721 (2010).

[2] B. Tudu and A. Tiwari, Recent developments in perpendicular magnetic anisotropy thin films for data storage applications, Vacuum **146**, 329 (2017).

[3] J. S. Moodera, L. R. Kinder, T. M. Wong, and P. Meservey, Large Magnetoresistance at Room Temperature in Ferromagnetic Thin Film Tunnel Junctions, Phys. Rev. Lett. **74**, 3273 (1995).

[4] T. Chen, R. K. Dumas, A. Eklund, P. K. Muduli, A. Houshang, A. A. Awad, P. Dürrenfeld, B. G. Malm, A. Rusu, and J. Åkerman, Spin-torque and spin-Hall nano-oscillators, Proceedings of the IEEE **104**, 1919 (2016).

[5] S. S. P. Parkin, M. Hayashi, and L. Thomas, Magnetic domain-wall racetrack memory, Science **320**, 190 (2008).

[6] S. Emori, U. Bauer, S. M. Ahn, E. Martinez, and G. S. D. Beach, Current-driven dynamics of chiral ferromagnetic domain walls, Nat. Mater. **12**, 611 (2013).

[7] S. Vélez, J. Schaab, M. S. Wörnle, M. Müller, E. Gradauskaite, P. Welter, C. Gutgsell, C. Nistor, C. L. Degen, M. Trassin, M. Fiebig, and P. Gambardella, High-speed domain wall racetracks in a magnetic insulator, Nat. Commun. **10**, 4750 (2019).

[8] N. Nishimura, T. Hirai, A. Koganei, T. Ikeda, K. Okano, Y. Sekiguchi, and Y. Osada, Magnetic tunnel junction device with perpendicular magnetization films for high-density magnetic random access memory, J. Appl. Phys. **91**, 5246 (2002).

[9] J. Finley and L. Liu, Spin-orbit-torque Efficiency in Compensated Ferrimagnetic Cobalt-Terbium Alloys, Phys. Rev. Appl. **6**, 054001 (2016).

[10] G. Kim, Y. Sakuraba, M. Oogane, Y. Ando, and T. Miyazaki, Tunneling magnetoresistance of magnetic tunnel junctions using perpendicular magnetization $L1_0$-CoPt electrodes, Appl. Phys. Lett. **92**, 172502 (2008).

[11] S. Mangin, D. Ravelosona, J. A. Katine, M. J. Carey, B. D. Terris, and Eric E. Fullerton, Current-induced magnetization reversal in nanopillars with perpendicular anisotropy, Nat. Mater. **5**, 210 (2006).

[12] B. Carvello, C. Ducruet, B. Rodmacq, S. Auffret, E. Gautier, G. Gaudin, and B. Dieny, Sizable room-temperature magnetoresistance in cobalt based magnetic tunnel junctions with out-of-plane anisotropy, Appl. Phys. Lett. **92**, 102508 (2008).

[13] H. L. Wang, C. H. Du, P. C. Hammel, and F. Yang, Strain-tunable magnetocrystalline anisotropy in epitaxial $Y_3Fe_5O_{12}$ thin films, Phys. Rev. B. **89**, 134404 (2014).

[14] J. Ding, C. Liu, Y. Zhang, U. Erugu, Z. Quan, R. Yu, E. McCollum, S. Mo, S. Yang, H. Ding, X. Xu, J. Tang, X. Yang, and M. Wu, Nanometer-Thick Yttrium Iron Garnet Films with Perpendicular Anisotropy and Low Damping, Phys. Rev. Appl. **14**, 014017 (2020).

[15] L. Soumah, N. Beaulieu, L. Qassym, C. Carrétéro, E. Jacquet, R. Lebourgeois, J. Ben Youssef, P. Bortolotti, V. Cros, and A. Anane, Ultra-low damping insulating magnetic thin films get perpendicular, Nat. Commun. **9**, 3355 (2018).

[16] Q. Shao, C. Tang, G. Yu, A. Navabi, H. Wu, C. He, J. Li, P. Upadhyaya, P. Zhang, S. A. Razavi, *et al.*, Role of dimensional crossover on spin-orbit torque efficiency in magnetic insulator thin films, Nat. Commun. **9**, 3612 (2018).

[17] C. O. Avci, A. Quindeau, C.-F. Pai, M. Mann, L. Caretta, A. S. Tang, M. C. Onbasli, C. A. Ross, and G. S. D. Beach, Current-induced switching in a magnetic insulator, Nat. Mater. **16**, 309 (2017).

[18] A. J. Lee, A. S. Ahmed, J. Flores, S. Guo, B. Wang, N. Bagués, D. W. McComb, and F. Yang, Probing the Source of the Interfacial Dzyaloshinskii-Moriya Interaction Responsible for the Topological Hall Effect in Metal/$Tm_3Fe_5O_{12}$ Systems, Phys. Rev. Lett. **124**, 107201 (2020).

[19] P. Li, J. Kally, S. S.-L. Zhang, T. Pillsbury, J. Ding, G. Csaba, J. Ding, J. S. Jiang, Y. Liu, R. Sinclair, *et al.*, Magnetization switching using topological surface states, Sci. Adv. **5**, eaaw3415 (2019).

[20] Y. Kajiwara, K. Harii, S. Takahashi, J. Ohe, K. Uchida, M. Mizuguchi, H. Umezawa, H. Kawai, K. Ando, K. Takanashi, S. Maekawa, and E. Saitoh, Transmission of electrical signals by spin-wave interconversion in a magnetic insulator, Nature **464**, 262 (2010).

[21] R. Lebrun, A. Ross, S. A. Bender, A. Qaiumzadeh, L. Baldrati, J. Cramer, A. Brataas, R. A. Duine, and M. Kläui, Tunable long-distance spin transport in a crystalline antiferromagnetic iron oxide, Nature **561**, 222 (2018).

[22] L. J. Cornelissen, J. Liu, R. A. Duine, J. Ben Youssef, and B. J. Van Wees, Long distance transport of magnon spin information in a magnetic insulator at room temperature, Nat. Phys. **11**, 1022 (2015).

[23] S. Chatterjee, J. F. Rodriguez-Nieva, and E. Demler, Diagnosing phases of magnetic insulators via noise magnetometry with spin qubits, Phys. Rev. B **99**, 104425 (2019).

[24] P. Upadhyaya, P. K. Amiri, A. A. Kovalev, Y. Tserkovnyak, G. Rowlands, Z. Zeng, I. Krivorotov, H. Jiang, and K. L. Wang, Thermal stability characterization of magnetic tunnel junctions using hard-axis magnetoresistance measurements, J. Appl. Phys. **109**, 07C708 (2011).

[25] J. Holanda, D. S. Maior, A. Azevedo, and S. M. Rezende, Detecting the phonon spin in magnon-phonon conversion experiments, Nat. Phys. **14**, 500 (2018).

[26] K. An, K. S. Olsson, A. Weathers, S. Sullivan, X. Chen, X. Li, L. G. Marshall, X. Ma, N. Klimovich, J. Zhou, L. Shi, and X. Li, Magnons and Phonons Optically Driven out of Local Equilibrium in a Magnetic Insulator, Phys. Rev. Lett. **117**, 107202 (2016).

[27] S. O. Demokritov, V. E. Demidov, O. Dzyapko, G. A. Melkov, A. A. Serga, B. Hillebrands, and A. N. Slavin, Bose-Einstein condensation of quasi-equilibrium magnons at room temperature under pumping, Nature **443**, 430 (2006).

[28] C. H. Du, T. Van der Sar, T. X. Zhou, P. Upadhyaya, F. Casola, H. Zhang, M. C. Onbasli, C. A. Ross, R. L. Walsworth, Y. Tserkovnyak, and A. Yacoby, Control and local measurement of the spin chemical potential in a magnetic insulator, Science **357**, 195 (2017).

[29] M. R. Page, B. A. McCullian, C. M. Purser, J. G. Schulze, T. M. Nakatani, C. S. Wolfe, J. R. Childress, M. E. McConney, B. M. Howe, P. C. Hammel, and V. P. Bhallamudi, Optically detected ferromagnetic resonance in metallic ferromagnets via nitrogen vacancy centers in diamond, J. Appl. Phys. **126**, 124902 (2019).

[30] B. Flebus and Y. Tserkovnyak, Quantum-impurity Relaxometry of Magnetization Dynamics, Phys. Rev. Lett. **121**, 187204 (2018).

[31] J. F. Rodriguez-Nieva, D. Podolsky, and E. Demler, Hydrodynamic sound modes and viscous damping in a magnon fluid, arXiv:1810.12333 [cond-mat.mes-hall] (2020).

[32] S. Foner, Versatile and sensitive vibrating-sample magnetometer, Rev. Sci. Instrum. **30**, 548 (1959).

[33] M. Buchner, K. Höfler, B. Henne, V. Ney, and A. Ney, Tutorial: Basic principles, limits of detection, and pitfalls of highly sensitive SQUID magnetometry for nanomagnetism and spintronics, J. Appl. Phys. **124**, 161101 (2018).

[34] C. Kittel, On the theory of ferromagnetic resonance absorption, Phys. Rev. **73**, 155 (1948).

[35] W. Jiang, P. Upadhyaya, W. Zhang, G. Yu, M. B. Jungfleisch, F. Y. Fradin, J. E. Pearson, Y. Tserkovnyak, K.

L. Wang, O. Heinonen, *et al.*, Blowing magnetic skyrmion bubbles, Science **349**, 283 (2015).

[36] B. Huang, G. Clark, E. Navarro-Moratalla, D. R. Klein, R. Cheng, K. L. Seyler, D. Zhong, E. Schmidgall, M. A. McGuire, D. H. Cobden, *et al.*, Layer-dependent ferromagnetism in a van der Waals crystal down to the monolayer limit, Nature **546**, 270 (2017).

[37] Y. Li, N. Sinitsyn, D. L. Smith, D. Reuter, A. D. Wieck, D. R. Yakovlev, M. Bayer, and S. A. Crooker, Intrinsic Spin Fluctuations Reveal the Dynamical Response Function of Holes Coupled to Nuclear Spin Baths in (In, Ga) as Quantum Dots, Phys. Rev. Lett. **108**, 186603 (2012).

[38] A. Murayama, K. Hyomi, J. Eickmann, and C. M. Falco, Brillouin study of long-wavelength spin waves in quasimonatomic Co films with uniaxial perpendicular magnetic anisotropy, Phys. Rev. B **61**, 8984 (2000).

[39] L. Rondin, J.-P. Tetienne, T. Hingant, J.-F. Roch, P. Maletinsky, and V. Jacques, Magnetometry with nitrogen-vacancy defects in diamond, Reports Prog. Phys. **77**, 056503 (2014).

[40] G. Kucsko, P. C. Maurer, N. Y. Yao, M. Kubo, H. J. Noh, P. K. Lo, H. Park, and M. D. Lukin, Nanometre-scale thermometry in a living cell, Nature **500**, 54 (2013).

[41] S. J. Devience, L. M. Pham, I. Lovchinsky, A. O. Sushkov, N. Bar-Gill, C. Belthangady, F. Casola, M. Corbett, H. Zhang, M. Lukin, *et al.*, Nanoscale NMR spectroscopy and imaging of multiple nuclear species, Nat. Nanotechnol. **10**, 129 (2015).

[42] J. R. Maze, P. L. Stanwix, J. S. Hodges, S. Hong, J. M. Taylor, P. Cappellaro, L. Jiang, M. V. Gurudev Dutt, E. Togan, A. S. Zibrov, *et al.*, Nanoscale magnetic sensing with an individual electronic spin in diamond, Nature **455**, 644 (2008).

[43] F. Casola, T. van der Sar, and A. Yacoby, Probing condensed matter physics with magnetometry based on nitrogen-vacancy centres in diamond, Nat. Rev. Mater. **3**, 17088 (2018).

[44] P. Neumann, I. Jakobi, F. Dolde, C. Burk, R. Reuter, G. Waldherr, J. Honert, T. Wolf, A. Brunner, J. H. Shim, *et al.*, High-precision nanoscale temperature sensing using single defects in diamond, Nano Lett. **13**, 2738 (2013).

[45] G. Balasubramanian, I. Y. Chan, R. Kolesov, M. Al-Hmoud, J. Tisler, C. Shin, C. Kim, A. Wojcik, P. R. Hemmer, A. Krueger, *et al.*, Nanoscale imaging magnetometry with diamond spins under ambient conditions, Nature **455**, 648 (2008).

[46] X. Wang, Y. Xiao, C. Liu, E. Lee-Wong, N. J. McLaughlin, H. Wang, M. Wu, H. L. Wang, E. E. Fullerton, and C. H. R. Du, Electrical control of coherent spin rotation of a single-spin qubit, npj Quantum Inf. **6**, 78 (2020).

[47] P. Andrich, C. F. de las Casas, X. Liu, H. L. Bretscher, J. R. Berman, F. J. Heremans, P. F. Nealey, and D. D. Awschalom, Long-range spin wave mediated control of defect qubits in nanodiamonds, npj Quantum Inf. **3**, 28 (2017).

[48] E. R. MacQuarrie, T. A. Gosavi, N. R. Jungwirth, S. A. Bhave, and G. D. Fuchs, Mechanical Spin Control of Nitrogen-Vacancy Centers in Diamond, Phys. Rev. Lett. **111**, 227602 (2013).

[49] D. Labanowski, V. P. Bhallamudi, Q. Guo, C. M. Purser, B. A. McCullian, P. C. Hammel, and S. Salahuddin, Voltage-driven, local, and efficient excitation of nitrogen-vacancy centers in diamond, Sci. Adv. **4**, eaat6574 (2018).

[50] D. Kikuchi, D. Prananto, K. Hayashi, A. Laraoui, N. Mizuochi, M. Hatano, E. Saitoh, Y. Kim, C. A. Meriles, and T. An, Long-distance excitation of nitrogen-vacancy centers in diamond via surface spin waves, Appl. Phys. Express **10**, 103004 (2017).

[51] M. Pelliccione, A. Jenkins, P. Ovartchaiyapong, C. Reetz, E. Emmanouilidou, N. Ni, and A. C. Bleszynski Jayich, Scanned probe imaging of nanoscale magnetism at cryogenic temperatures with a single-spin quantum sensor, Nat. Nanotechnol. **11**, 700 (2016).

[52] L. Thiel, Z. Wang, M. A. Tschudin, D. Rohner, I. Gutiérrez-Lezama, N. Ubrig, M. Gibertini, E. Giannini, A. F. Morpurgo, and P. Maletinsky, Probing magnetism in 2D materials at the nanoscale with single-spin microscopy, Science **364**, 973 (2019).

[53] R. D. McMichael, D. J. Twisselmann, and A. Kunz, Localized Ferromagnetic Resonance in Inhomogeneous Thin Films, Phys. Rev. Lett. **90**, 227601 (2003).

[54] J. M. Shaw, H. T. Nembach, and T. J. Silva, Determination of spin pumping as a source of linewidth in sputtered $\mathrm{Co}_{90}\mathrm{Fe}_{10}/\mathrm{Pd}$ multilayers by use of broadband ferromagnetic resonance spectroscopy, Phys. Rev. B. **85**, 054412 (2012).

[55] M. J. Burek, N. P. de Leon, B. J. Shields, B. J. M. Hausmann, Y. Chu, Q. Quan, A. S. Zibrov, H. Park, M. D. Lukin, and M. Lončar, Free-standing mechanical and photonic nanostructures in single-crystal diamond, Nano Lett. **12**, 6084 (2012).

[56] E. Lee-Wong, R. L. Xue, F. Y. Ye, A. Kreisel, T. van der Sar, A. Yacoby, and C. H. R. Du, Nanoscale detection of magnon excitations with variable wavevectors through a quantum spin sensor, Nano Lett. **20**, 3284 (2020).

[57] T. van der Sar, F. Casola, R. Walsworth, and Amir Yacoby, Nanometre-scale probing of spin waves using single-electron spins, Nat. Commun. **6**, 7886 (2015).

[58] J. P. Tetienne, T. Hingant, L. Rondin, A. Cavaillès, L. Mayer, G. Dantelle, T. Gacoin, J. Wrachtrup, J.-F. Roch, and V. Jacques, Spin relaxometry of single nitrogen-vacancy defects in diamond nanocrystals for magnetic noise sensing, Phys. Rev. B. **87**, 235436 (2013).

[59] T. Nozaki, Y. Shiota, S. Miwa, S. Murakami, F. Bonell, S. Ishibashi, H. Kubota, K. Yakushiji, T. Saruya, A. Fukushima, *et al.*, Electric-field-induced ferromagnetic resonance excitation in an ultrathin ferromagnetic metal layer, Nat. Phys. **8**, 491 (2012).

[60] A. B. Solanki, S. I. Bogdanov, A. Rustagi, N. R. Dilley, T. Shen, M. M. Rahman, W. Tong, P. Debashis, Z. Chen, J. Appenzeller, *et al.*, Electric field control of interaction between magnons and quantum spin defects, arXiv:2012.01497 [cond-mat.mes-hall] (2020).

[61] L. Trifunovic, F. L. Pedrocchi, and D. Loss, Long-Distance Entanglement of Spin Qubits via Ferromagnet, Phys. Rev. X. **3**, 041023 (2013).

[62] C. M. Srivastava and R. Aiyar, Spin wave stiffness constants in some ferrimagnetics, J. Phys. C. Solid State Phys. **20**, 1119 (1987).

[63] A. J. Lee, A. S. Ahmed, J. Flores, S. Guo, B. Wang, N. Bagués, D. W. McComb, and F. Yang, Interfacial Rashba-Effect-Induced Anisotropy in Nonmagnetic-Material-Ferrimagnetic-Insulator Bilayers, Phys. Rev. Lett. **124**, 257202 (2020).

[64] C. Du, R. Adur, H. L. Wang, A. J. Hauser, F. Yang, and P. C. Hammel, Control of Magnetocrystalline Anisotropy by Epitaxial Strain in Double Perovskite Sr_2FeMoO_6 Films, Phys. Rev. Lett. **110**, 147204 (2013).

[65] B. A. Kalinikos and A. N. Slavin, Ferromagnetic films with mixed exchange boundary conditions, J. Phys. C: Solid State Phys. **19**, 7013 (1986).